Environmental Science
Water Research & Technology

PAPER

View Article Online
View Journal | View Issue

Published on 11 January 2023. Downloaded by National Synchrotron Radiation Research on 3/18/2024 4:37:23 AM.

Check for updates

Cite this: *Environ. Sci.: Water Res. Technol.*, 2023, **9**, 883

# Capacitive deionization and disinfection of saltwater using nanostructured (Cu–Ag)@C/rGO composite electrodes

W.-T. Chang,[a] P.-A. Chen,[a] C.-Y. Peng,[b] S.-H. Liu[a] and H. Paul Wang*[a]

Received 31st July 2022,
Accepted 8th January 2023

DOI: 10.1039/d2ew00584k

rsc.li/es-water

Fresh water shortage is an urgent worldwide problem that needs to be solved. Thus, the main objective of this work was to prepare new nanostructured electrodes for capacitive deionization (CDI) of saltwater with an additional disinfection step to produce fresh water or potential drinking water. Graphene is a two-dimensional carbon with high electrical conductivity and a disinfection ability comparable with nano silver and copper. The (Cu–Ag)@C core–shell nanoparticles were prepared by carbonization of $Ag^{+}$-β-cyclodextrin-$Cu^{2+}$ complexes at 673 K for 4 h. The bimetallic Cu–Ag nanoparticles were encapsulated within a carbon-shell, which was dispersed in reduced graphene oxide (rGO) to form (Cu–Ag)@C/rGO composites which acted as the CDI electrode materials. Mainly nano Ag (98–100%) was coated on relatively inexpensive copper in the (Cu–Ag)@C nanoparticles for simultaneous desalination and disinfection. From *in situ* SAXS, the particle sizes of the (Cu–Ag)@C were in the range of 42–52 nm. More defects and a higher specific capacitance of the (Cu–Ag)@C/rGO composites were observed by Raman spectroscopy and electrochemical analysis (cyclic voltammetry curves (CV)), respectively. The desalination performances associated with the electrosorption efficiencies (21–38%), electrosorption capacities (21–33 mg $g^{-1}$) and optimized salt removals (504–792 mg $g^{-1}$ per day) of the composite electrodes in the once-through, four cycles (repeated electrosorption and regeneration under +1.2 and −1.2 V, respectively) CDI processes were greatly improved with a stable recycling performance of 10 h. In addition, the composites have high disinfection efficiencies (79–90%). The unique (Cu–Ag)@C/rGO composite electrodes showed great desalination performances and disinfection efficiencies, and can thus be used for water recycling/reuse, and potentially drinking water, from saltwater, inorganic wastewater and contaminated groundwater.

**Water impact**

New (Cu–Ag)@C core–shell nanoparticles on rGO composite electrodes have been prepared for capacitive deionization of saltwater with an additional function of disinfection. Their high desalination performances and disinfection efficiencies enable water recycling/reuse for the potential generation of drinking water from saltwater, inorganic wastewater and contaminated groundwater.

## 1. Introduction

Freshwater only accounts for 2.5% of the earth water's storage whereas the majority is seawater (97%).[1,2] Seawater is, therefore, becoming the main water resource for freshwater. Reverse osmosis membranes, electrodialysis, multi-effect distillation and multi-stage flash desalination methods have been widely used to provide freshwater to millions of people around the world.[3–6] However, they all have common drawbacks of high cost and high energy consumption. For water softening applications, divalent ions (>85%) can be removed from saltwater by the relatively simple capacitive deionization (CDI) method.[7,8] In general, CDI has the advantages of relatively low energy consumption and environment friendliness.[9–11] In the CDI process, saltwater can be deionized by applying an electrical field between a pair of oppositely-charge electrodes. Hence, the electrostatic adsorption is the driving force for ion transport in CDI. Anions and cations are forced to move to opposite-charge electrodes, and stored in the electrical double layer (EDL) on the electrodes.[12–14]

Carbons such as activated carbon (AC), carbon aerogels, carbon nanotubes, carbon fibers and graphene, having a high surface area and porous structure, have been widely used for CDI electrode materials.[15–18] Graphene with a two-

[a] *Department of Environmental Engineering, National Cheng Kung University, Tainan 70101, Taiwan. E-mail: wanghp@ncku.edu.tw*
[b] *Department of Water Resources and Environmental Engineering, Tamkang University, New Taipei City 25137, Taiwan*

Published on 11 January 2023. Downloaded by National Synchrotron Radiation Research on 3/18/2024 4:37:23 AM.

dimensional carbon containing a single layer of $sp^2$ carbon hybridization with a very high electrical conductivity, thermal conductivity and mechanical strength has gained great attention and wide use in practical applications.[19–21] Graphene is also an effective disinfection material with a severe cytotoxic effect on bacteria, fungi and plant pathogens.[22] The disinfection action of graphene involves physical damage which is induced mainly by the direct contact of the sharp edges with bacterial membranes and destructive extraction of the lipid molecules.[23,24]

Nano silver has a relatively high disinfection ability for infectious microorganisms.[25] Many products exploit nano silver composites as disinfection agents, ranging from water filters to clothing.[26,27] Nano silver has different and tunable physical and chemical properties including size, shape and surface chemistry.[28,29] Also, silver nanoparticles coated with a carbon-shell (Ag@C) can enhance biocompatibility in aqueous solutions.[30,31] Compared with other chemical disinfection agents, silver has less toxicity.[32,33] Copper which is relatively inexpensive also has a disinfection ability using copper-mediated reactive oxygen species.[34,35]

A simple method for preparing nanosize-controllable metals (such as Ag, Cu, Fe, and Ni) encapsulated within a porous carbon-shell (M@C) by carbonization of metal ion-β-cyclodextrin (CD) complexes at 673 K has been developed in our laboratory.[31] Aggregation and oxidation of the core metals in the core–shell nanoparticles can be lessened by the carbon shell.[36–38] In addition, the high electrical conductivity carbon-shell that can reduce the interface resistance of the electron transport has a pore opening of approximately 0.5 nm which allows ions to freely diffuse in and out.[32] Thus, the main objective of this work was to prepare new core–shell nanoparticles, particularly silver–copper bimetallic nanostructures that could offer synergistic features over mono metals to achieve the goals of higher efficiency and lower cost. The core–shell nanoparticles were dispersed on rGO to serve as the electrode materials for the desired desalination performance, with an additional function of disinfection, for the CDI of saltwater to freshwater, and potentially drinking water.

## 2. Materials and methods

Briefly, copper(II) nitrate ($Cu(NO_3)_2{\cdot}2.5\ H_2O$, JT Baker) and silver(I) nitrate ($AgNO_3$, (99%) Sigma) at the $X_{Ag}$ (Ag/(Ag + Cu)) molar fractions of 0–1 were chelated with β-cyclodextrin (CD) at a (CD/(Ag + Cu)) molar ratio of 6. The $Cu^{2+}$–CD–$Ag^{+}$ complexes were dried at 353 K for 16 h, and then carbonized in a high-purity $N_2$ gas at 673 K for 4 h to form the nanostructured bimetallic Cu and Ag encapsulated within the carbon-shell (core–shell nanoparticles).

Graphene oxide (GO) was prepared using the Hummers method.[39] A graphite slice (1 g) was mixed with sulfuric acid ($H_2SO_4$, Sigma) (80 mL), sodium nitrate ($NaNO_3$, Hanawa) (1.6 g), and potassium permanganate ($KMnO_4$, Sigma) (7.5 g) in water at 368 K for 24 h. The graphite solution was diluted with deionized water (200 mL) at 353–368 K. Hydrogen peroxide ($H_2O_2$, 30%, Sigma,) (30 mL) was added to the graphite solution until the color of the solution became golden yellow. Extra metal ions were removed by HCl (37%, Sigma) (20 mL). The GO was reduced to reduced graphene oxide (rGO) with hexamethylenetetramine at 368 K for 3 h.

A very small amount of Ag ($X_{Ag}$ = 0.33–0.67) was used in the preparation of the Cu–Ag bimetallic nanostructure (Ag coated on a relatively low cost Cu (Cu@Ag)) encapsulated within a porous carbon-shell to form (Cu–Ag)@C ((Cu + Ag)/C = 10%) core–shell nanoparticles that were highly dispersed in rGO ((Cu + Ag)@C/rGO = 10% approximately). After filtration, the (Cu–Ag)@C/rGO composite were coated on a graphite sheet for use as the CDI electrodes.

The desalination performance of the experiments was determined between eight parallel electrodes and each electrode had an area of 2.5 × 2.5 $cm^2$ under +1.2 and −1.2 V for electrosorption and regeneration, respectively. The desalination performance (related to electrosorption capacity (EC), optimized salt removal (OSR) and recycling performance) for the CDI of a simulated saltwater ([NaCl] = 50 ppm) using the composite electrodes was determined by monitoring its electrical conductivity changes normalized to concentrations. The EC (mg $g^{-1}$) was determined by ΔC·V/W (where ΔC is concentration difference (mg $L^{-1}$), $V$ is saltwater volume ($L$) and $W$ is composite weight (g)). The OSR (mg $g^{-1}$ per day) represents the amount (mg) of salt removed per gram of the composite during a predetermined operational time (day).

The specific capacitances of the electrodes were measured by CV in a three-electrode system in a NaCl aqueous solution (0.1 M) at a scan rate of 25 mV $s^{-1}$ between −0.6 V and +0.6 V. The Ag/AgCl and platinum (wire) were used as the reference and counter electrodes, respectively. Their specific capacitances (F $g^{-1}$) were determined by $C = S/2vm$ (where $S$ is the area of the CV (V·A), m is the weight (g) of the composite coated on graphite, and $v$ is the scan rate (V/s)).

The chemical structure of the core–shell nanoparticles was studied using X-ray diffraction (XRD) (Bruker, D8 Advance) at a scan rate of 5° $min^{-1}$ under the working voltage of 40 kV (40 mA). Speciation of copper and silver in the core–shell nanoparticles was determined using synchrotron X-ray absorption near edge structure (XANES) spectroscopy at the Taiwan National Synchrotron Radiation Research Center (NSRRC). A Si(111) double-crystal monochromator was used for energy selection at an energy resolution ($\Delta E/E$) of $1.9 \times 10^{-4}$ (eV/eV). Their bond distances and coordination numbers (CNs) were also determined using extended X-ray absorption fine structure (EXAFS) and analysis by the IFEFFIT programs. The small angle X-ray scattering (SAXS) spectra of the core–shell nanoparticles were obtained using the SAXS BL23A beam line at NSRRC. The SAXS spectra with the elastic scattering of X-rays could provide more sensitivity for chemical structures as well as the particle size and shape of the nanoparticles. The *in situ* SAXS spectra for the formation of the core–shell nanoparticles were determined at 300–600 K.

 This journal is © The Royal Society of Chemistry 2023

Published on 11 January 2023. Downloaded by National Synchrotron Radiation Research on 3/18/2024 4:37:23 AM.

The *Escherichia coli* was grown in the Luria-Bertani medium (LB, Becton Dickinson) at 310 K for 24 h, and the bacterial suspension was diluted with the LB broth medium to concentrations of 106–107 cfu $mL^{-1}$. For the disk-diffusion test, using the Kirby–Bauer method, the (Cu–Ag)@C/rGO composite dispersed aqueous solution was added to the LB agar (agar granulated, Becton Dickinson) plates with *E. coli* spread over it. The plates were incubated at 310 K for 24 h, and the inhibition zones were measured. The minimum inhibitory concentration (MIC) was determined in a NaCl aqueous solution that was also used for CDI. An aliquot of about 100 μL was spread onto the LB agar plates and incubated at 310 K for 24 h. The disinfection efficiency was determined by counting the number ($N$) of colonies, *i.e.*, disinfection efficiency (%) = 100% ($N_{control} - N_{sample}$)/$N_{control}$.

## 3. Results and discussion

The XRD patterns of the (Cu–Ag)@C core–shell nanoparticles having $X_{Ag}$ (0–1) and the corresponding PDF standard patterns of Ag (PDF 04-0783) and Cu (PDF 04-0836) are shown in Fig. 1. The broadened feature at 10–40° (2$\theta$) could be attributed to the amorphous carbon-shell. The XRD peaks at 38.2° (Ag(111)), 44.35° (Ag(200)), 64.4° (Ag(220)) and 77.4° (Ag(311)) were associated with the existence of nano Ag. The nano Cu peaks centered at 43.3°, 50.4° and 74.1° could be assigned to Cu(111), Cu(200) and Cu(220), respectively. It was clear that nano Ag and Cu existed in the (Cu–Ag)@C composite without formation of a AgCu alloy.

The K-edge XANES spectra of copper and silver in the (Cu–Ag)@C core–shell nanoparticles having the $X_{Ag}$ fractions of 0.33–0.67 are shown in Fig. 2. The main copper species in the (Cu–Ag)@C were Cu (40–45%), $Cu_2O$ (28–30%) and CuO (18–34%), and mainly nano Ag (98–100%) was observed. In Table 1, the Ag–Ag bond distances, obtained by EXAFS, for the (Cu–Ag)@C core–shell nanoparticles are shown to be in the range of 2.85–2.86 Å with CNs of 8.0–8.6. The Cu–Cu (2nd shell) bond distances (2.55–2.56 Å) are not perturbed by the presence of Ag, and the copper had fewer CNs (3.3–5.1) than Ag, suggesting that the Ag may be relatively enriched on the surfaces of the bimetal Cu–Ag for the possible formation of Cu@Ag (Ag coated on Cu).

The growth of the (Cu–Ag)@C nanoparticles during the temperature-programmed carbonization of the $Cu^{2+}$–CD–$Ag^{+}$ complexes at 300–600 K was also determined by *in situ* synchrotron SAXS spectroscopy. In Fig. 3, the change of $I(Q)$ indicated that the characteristic size ranging from crystallographic distances (few Å) to colloidal sizes can be observed when the carbonization temperatures were increased to 600 K. At $T > 393$ K, the surface interaction of the nanoparticles could be seen. Formation of the (Cu–Ag)@C bimetal core–shell nanoparticles could be observed at $T > 450$ K.

Adsorption/desorption isotherms, specific surface areas and particle size distribution of the (Cu–Ag)@C/rGO

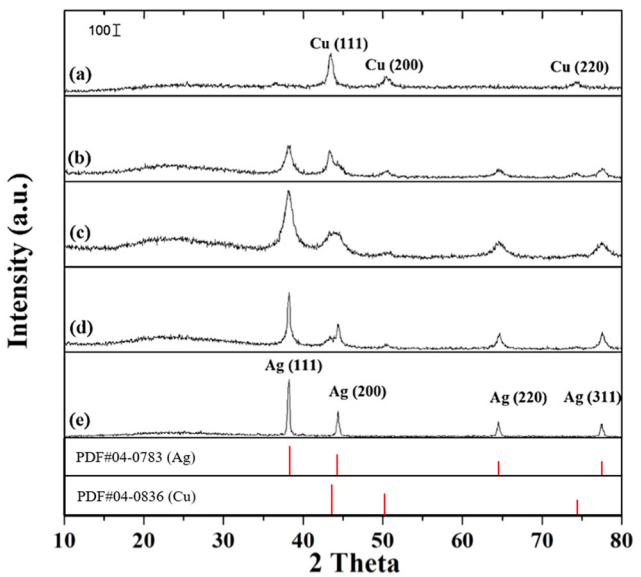


Fig. 1 The XRD patterns of the (Cu–Ag)@C core–shell nanoparticles with the $X_{Ag}$ of (a) 0, (b) 0.33, (c) 0.50, (d) 0.67 and (e) 1.0. The corresponding PDF standard patterns of Cu and Ag are also included.

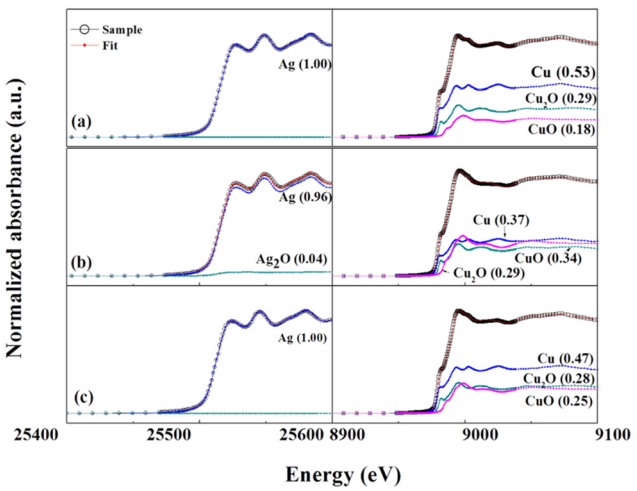


Fig. 2 Component fitted XANES spectra of copper and silver in the (Cu–Ag)@C core–shell nanoparticles with $X_{Ag}$ of (a) 0.33, (b) 0.50 and (c) 0.67.

Table 1 Speciation parameters of silver and copper in the (Cu–Ag)@C core–shell nanoparticles studied by EXAFS, and the Raman intensity ratios of the D-to-G bands ($I_D/I_G$), electrosorption capacities (EC) (mg $g^{-1}$) and disinfection efficiencies (D) (%)

| $X_{Ag}$ | 2nd shells | $R$ | CN | $\sigma^2$ | $I_D/I_G$ | EC | $D$ |
|---|---|---|---|---|---|---|---|
| 0.33 | Ag–Ag | 2.86 | 8.0 | 0.0104 | 0.96 | 21 | 83 |
| | Cu–Cu | 2.55 | 4.4 | 0.0096 | | | |
| 0.50 | Ag–Ag | 2.86 | 8.1 | 0.0099 | 1.2 | 33 | 90 |
| | Cu–Cu | 2.56 | 3.3 | 0.0095 | | | |
| 0.67 | Ag–Ag | 2.86 | 8.6 | 0.0105 | 1.2 | 28 | 79 |
| | Cu–Cu | 2.55 | 5.0 | 0.0098 | | | |

CN: coordination number, $R$: bond distance (Å), $\sigma^2$: Debye–Waller factor, $X_g$: Ag fraction (Ag/(Ag + Cu)).

Published on 11 January 2023. Downloaded by National Synchrotron Radiation Research on 3/18/2024 4:37:23 AM.

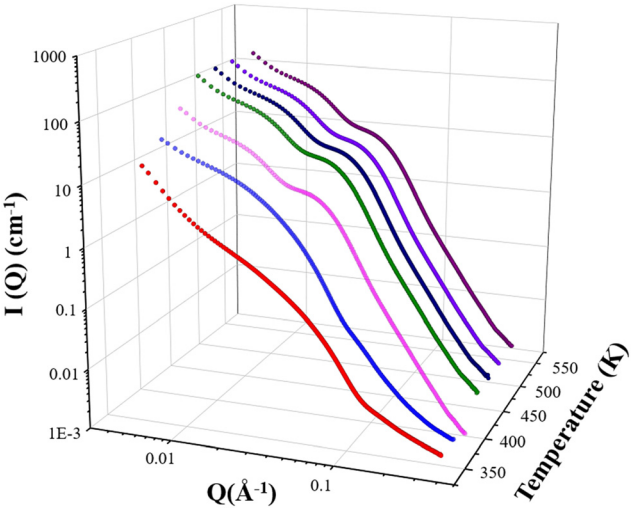


Fig. 3 *In situ* synchrotron SAXS profiles during temperature-programmed carbonization of the $Cu^{2+}$-β-cyclodextrin-$Ag^{+}$ complexes at 300–600 K.

composite are shown in Fig. 4. The specific surface area of the (Cu–Ag)@C/rGO with the $X_{Ag}$ of 0.33, 0.50 and 0.67 were 825, 1219 and 1070 $m^2$ $g^{-1}$, respectively. The particle sizes of the (Cu–Ag)@C core–shell nanoparticles were in the range of 42–52 nm.

The TEM images in Fig. 5(A) show that the core–shell nanoparticles are well dispersed on the two dimensional rGO sheets that were dark and wrinkled. In Fig. 5(B), the chemical structure of the (Cu–Ag)@C/rGO composite and graphite was also studied by Raman spectroscopy. Two prominent features at 1350 and 1590 $cm^{-1}$ represent the D and G bands, respectively. The D band may be associated with the first-order scattering of the zone-boundary phonons, which is usually assigned to the defect sheet yielding the scattering signal of the rGO. The G band corresponds to the ordered

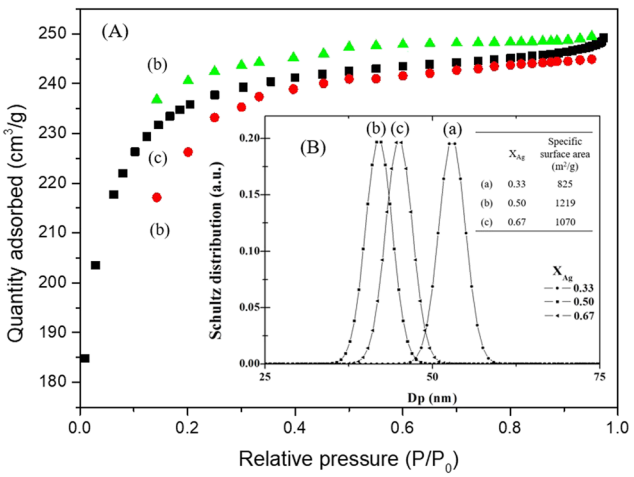


Fig. 4 (A) Adsorption/desorption isotherms and (B) pore size distributions (Schultz distributions) of the (Cu–Ag)@C core–shell nanoparticles with the $X_{Ag}$ of (a) 0.33, (b) 0.50 and (c) 0.67. Their specific surface areas are also shown in the inset.

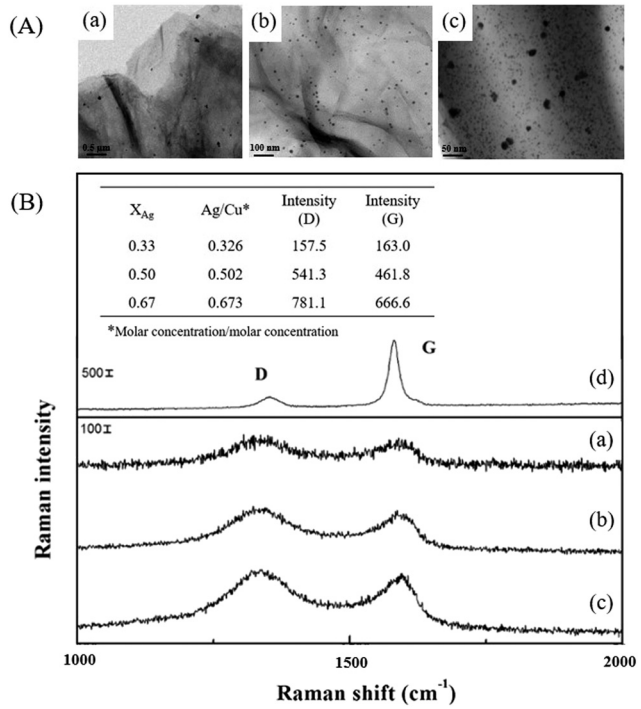


| $X_{Ag}$ | Ag/Cu* | Intensity (D) | Intensity (G) |
|---|---|---|---|
| 0.33 | 0.326 | 157.5 | 163.0 |
| 0.50 | 0.502 | 541.3 | 461.8 |
| 0.67 | 0.673 | 781.1 | 666.6 |

*Molar concentration/molar concentration

Fig. 5 (A) The TEM images, and (B) the Raman spectra of the (Cu–Ag)@C/rGO core–shell nanoparticles with $X_{Ag}$ of (a) 0.33, (b) 0.50 and (c) 0.67, and (d) graphite. Their D and G bond intensities are shown in the inset.

$sp^2$-bonded carbon atoms of rGO.[40] For example, the sharp peak of the G band in Fig. 5(d) indicated that the graphite had an $sp^2$ structure. In Table 1, the $I_D/I_G$ data (the intensity ratio of the D to G bands) could be an indicator of the increase in defects and disordered graphene layers. The (Cu–Ag)@C/rGO composite had greater D band intensities, which indicated the existence of more porous structure (see Fig. 5(a)–(c)). The (Cu–Ag)@C/rGO composite containing a smaller $X_{Ag}$ (0.33) had a greater intensity ratio ($I_D/I_G$), which may be associated with the presence of more defects.

The electrosorption and specific capacitance of the (Cu–Ag)@C/rGO composite were determined using CV. The specific capacitances of the rGO and (Cu–Ag)@C/rGO composite ($X_{Ag}$ = 0.33–0.67) electrodes are shown in Fig. 6. The rGO electrode has a specific capacitance of 493 F $g^{-1}$. It should be noted that the specific capacitances of the electrodes were increased in the presence of (Cu–Ag)@C nanoparticles. The (Cu–Ag)@C/rGO composite electrodes had relatively high specific capacitances of 544–716 F $g^{-1}$ for the high electrosorption efficiencies.

The electrosorption efficiencies for the four cycles of electrosorption and regeneration with the (Cu–Ag)@C/rGO composite electrodes are shown in Fig. 7. The (Cu–Ag)@C/rGO composite at the $X_{Ag}$ of 0.50 had a better desalination performance. The average once-through electrosorption efficiency under +1.2 V for the (Cu–Ag)@C/rGO ($X_{Ag}$ = 0.50) composite reached 38% in the first cycle. When the voltage was reversed (−1.2 V), the electrodes could be regenerated in


This journal is © The Royal Society of Chemistry 2023

Published on 11 January 2023. Downloaded by National Synchrotron Radiation Research on 3/18/2024 4:37:23 AM.

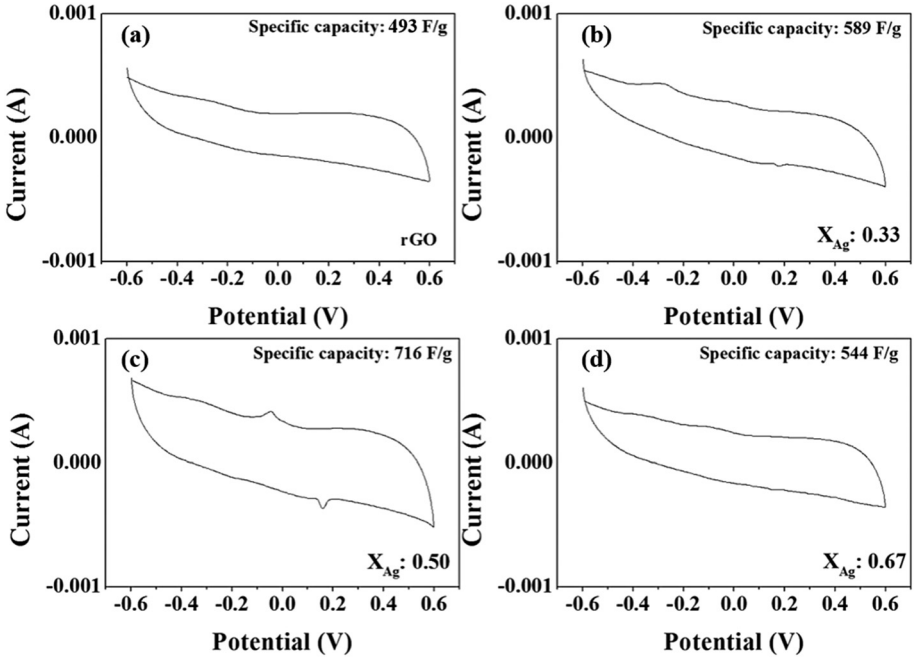


Fig. 6 The CV curves for the (a) rGO and (Cu–Ag)@C/rGO composite electrodes with the $X_{Ag}$ of (b) 0.33, (c) 0.50 and (d) 0.67.

a very short time. The electrosorption efficiency slightly decreased in the following cycles to 33% after a 10 h stability test (see the inset in Fig. 7). In addition, the (Cu–Ag)@C/rGO composite electrodes had approximately four times greater ECs (21–33 mg $g^{-1}$) than the rGO electrode, for the (Cu–Ag)@C/rGO ($X_{Ag}$ = 0.50) composite electrode. The better desalination performances of the (Cu–Ag)@C/rGO composite electrodes were also shown by their OSRs (504–792 mg $g^{-1}$ per day) that were much greater than that of the rGO electrode (192 mg $g^{-1}$ per day) (see the EC and OSR data in the inset of Fig. 7). A comparison of the CDI electrosorption efficiency and EC with other rGO-based electrodes is shown in Table 2. It was notable that the (Cu–Ag)@C/rGO ($X_{Ag}$ = 0.50) composite electrode also had a relatively high electrosorption efficiency and EC.

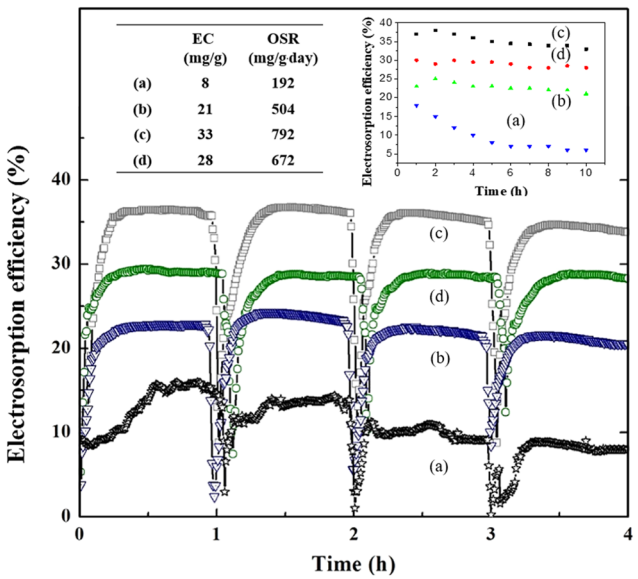


Fig. 7 The electrosorption efficiencies of the (a) rGO and (Cu–Ag)@C/rGO composite electrodes with $X_{Ag}$ of (b) 0.33, (c) 0.50 and (d) 0.67 under +1.2 and 0 V for electrosorption and regeneration, respectively. The insets show the EC (mg $g^{-1}$), OSR (mg $g^{-1}$ per day), and recycling performance of the composite electrodes for 10 h.

In Fig. 8, the inhibition zones are associated with the disinfection abilities of the (Cu–Ag)@C/rGO composites. The larger inhibition zones represent the greater disinfection ability of the composites. The inhibition zones clearly illustrate that the (Cu–Ag)@C/rGO composite with the $X_{Ag}$ of 0.33–0.67 had clear inhibition zones of 4–10 mm. The (Cu–Ag)@C/rGO composite ($X_{Ag}$ = 0.50) had a much greater disinfection ability than the others. The disinfection efficiencies related to the number of *E. coli* colonies during CDI are also shown in Table 2. The (Cu–Ag)@C/rGO composites at the $X_{Ag}$ of 0.33 and 0.50 performed well to control the *E. coli* colonies for 4 h. The disinfection efficiencies of the (Cu–Ag)@C/rGO composite with the $X_{Ag}$ of

Table 2 The electrosorption efficiency ($\varepsilon$) and electrosorption capacity (EC) of the rGO and core–shell nanoparticle dispersed rGO for flow-by CDI of saltwater under 1.2 V

| Electrode materials | $\varepsilon$ (%) | EC (mg $g^{-1}$) | Ref. |
|---|---|---|---|
| Purified rGO | 14 | 13 | Tuan *et al.*, 2015[41] |
| rGO | 23 | 22 | Chang and Hu, 2019[42] |
| Ag@C | 5.8 | 5.4 | Chang *et al.*, 2022[19] |
| Ag@C/rGO | 28 | 26 | Chang *et al.*, 2022[19] |
| (Cu–Ag)@C/rGO | 35 | 33 | This work |

$X_{Ag}$ = 0.50 for (Cu–Ag)@C.

Published on 11 January 2023. Downloaded by National Synchrotron Radiation Research on 3/18/2024 4:37:23 AM.

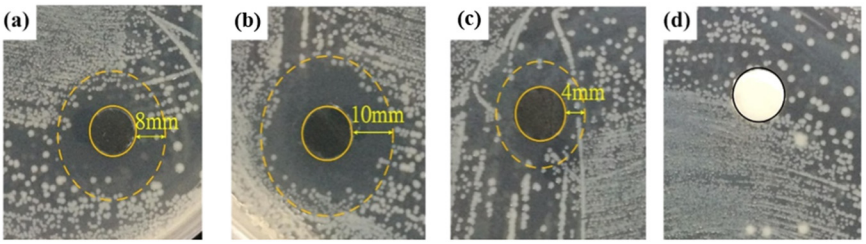


Fig. 8 Disinfection tests for the (Cu–Ag)@C/rGO composites with the $X_{Ag}$ of (a) 0.33, (b) 0.5, (c) 0.67 and (d) blank.

0.33–0.67 are 79–90%, similar to the results of the disk-diffusion test. Specifically, the (Cu–Ag)@C/rGO composite ($X_{Ag}$ = 0.50) had a better electrosorption and disinfection efficiency (see Table 1 and Fig. 7).

## 4. Conclusions

The K-edge XANES spectra of copper and silver in the (Cu–Ag)@C core–shell nanoparticles show the existence of mainly nano Ag (98–100%) coated on relatively inexpensive copper for use in simultaneous electrosorption and disinfection. Using *in situ* SAXS, the particle sizes of the (Cu–Ag)@C were in the range of 42–52 nm. More defects and a higher specific capacitance of the (Cu–Ag)@C/rGO composites that promoted the desalination performance were observed by Raman spectroscopy and electrochemical analysis (CV curves). The desalination performances associated with the electrosorption efficiencies (21–38%), electrosorption capacities (21–33 mg $g^{-1}$) and optimized salt removals (504–792 mg $g^{-1}$ per day) of the composite electrodes in the once-through CDI processes were highly improved with a stable recycling performance. In addition, the composites had high disinfection efficiencies (79–90%). These unique (Cu–Ag)@C core–shell nanoparticles dispersed on rGO showed the desired desalination performances and disinfection efficiencies, which demonstrated their potential for use in applications in water recycling, and reuse from saltwater, inorganic wastewater or contaminated groundwaters.

## Conflicts of interest

There are no conflicts of interest to declare.

## Acknowledgements

The financial support from the Taiwan Ministry of Science and Technology (Grant No. 108-2221-E-006-165-MY3, 109-2221-E-006-042-MY3 and 110-2221-E-006-107-MY2) is gratefully acknowledged.

## References

1 J. Bear, A. H.-D. Cheng, S. Sorek, D. Ouazar and I. Herrera, *Seawater intrusion in coastal aquifers: concepts, methods and practices*, Springer Science & Business Media, 1999.
2 V. Khilchevskyi and V. Karamushka, in *Clean Water and Sanitation*, Springer, 2021, pp. 1–11.
3 A. Panagopoulos, Techno-economic evaluation of a solar multi-effect distillation/thermal vapor compression hybrid system for brine treatment and salt recovery, *Chem. Eng. Process.*, 2020, **152**, 107934.
4 M. M. Aboelmaaref, M. E. Zayed, J. Zhao, W. Li, A. A. Askalany, M. S. Ahmed and E. S. Ali, Hybrid solar desalination systems driven by parabolic trough and parabolic dish CSP technologies: technology categorization, thermodynamic performance and economical assessment, *Energy Convers. Manage.*, 2020, **220**, 113103.
5 A. J. Toth, Modelling and Optimisation of Multi-Stage Flash Distillation and Reverse Osmosis for Desalination of Saline Process Wastewater Sources, *Membranes*, 2020, **10**, 265.
6 S. Lin, H. Zhao, L. Zhu, T. He, S. Chen, C. Gao and L. Zhang, Seawater desalination technology and engineering in China: A review, *Desalination*, 2021, **498**, 114728.
7 A. Kalfa, B. Shapira, A. Shopin, I. Cohen, E. Avraham and D. Aurbach, Capacitive deionization for wastewater treatment: Opportunities and challenges, *Chemosphere*, 2020, **241**, 125003.
8 J. Ahn, J. Lee, S. Kim, C. Kim, J. Lee, P. Biesheuvel and J. Yoon, High performance electrochemical saline water desalination using silver and silver-chloride electrodes, *Desalination*, 2020, **476**, 114216.
9 S. K. Mohamed, M. Abuelhamd, N. K. Allam, A. Shahat, M. Ramadan and H. M. Hassan, Eco-friendly facile synthesis of glucose-derived microporous carbon spheres electrodes with enhanced performance for water capacitive deionization, *Desalination*, 2020, **477**, 114278.
10 J. Ma, Y. Cheng, L. Wang, X. Dai and F. Yu, Free-standing $Ti_3C_2T_x$ MXene film as binder-free electrode in capacitive deionization with an ultrahigh desalination capacity, *Chem. Eng. J.*, 2020, **384**, 123329.
11 K. Elsaid, E. T. Sayed, M. A. Abdelkareem, M. S. Mahmoud, M. Ramadan and A. Olabi, Environmental impact of emerging desalination technologies: A preliminary evaluation, *J. Environ. Chem. Eng.*, 2020, **8**, 104099.
12 M. Abi Jaoude, E. Alhseinat, K. Polychronopoulou, G. Bharath, I. F. F. Darawsheh, S. Anwer, M. A. Baker, S. J. Hinder and F. Banat, Morphology-dependent electrochemical performance of $MnO_2$ nanostructures on graphene towards efficient capacitive deionization, *Electrochim. Acta*, 2020, **330**, 135202.
13 K. Z. Huang and H. L. Tang, Temperature and desorption mode matter in capacitive deionization process for water desalination, *Environ. Technol.*, 2020, **41**, 3456–3463.

 This journal is © The Royal Society of Chemistry 2023

Published on 11 January 2023. Downloaded by National Synchrotron Radiation Research on 3/18/2024 4:37:23 AM.

14 M. McKague, H. Fathiannasab, M. Agnaou, M. A. Sadeghi and J. Gostick, Extending pore network models to include electrical double layer effects in micropores for studying capacitive deionization, *Desalination*, 2022, **535**, 115784.
15 L. Men, C. Chen, A. Liu, S. Yu, J. Zhou, Y. Xie and D. Ju, N-doped porous carbon-based capacitive deionization electrode materials loaded with activated carbon fiber for water desalination applications, Journal of Environmental, *Chem. Eng.*, 2022, 107943.
16 A. F. Arangadi, J. K. Ali, M. Abi Jaoude, D. H. Anjum, A. AlKhoori, K. Polychronopoulou and E. Alhseinat, Role of embedding choline chloride-urea deep eutectic solvent on biomass-derived porous activated carbon in its capacitive deionization performance, *Desalination*, 2022, **530**, 115674.
17 S. Tian, Z. Zhang, X. Zhang and K. K. Ostrikov, Capacitative deionization using commercial activated carbon fiber decorated with polyaniline, *J. Colloid Interface Sci.*, 2019, **537**, 247–255.
18 S. Xiong, L. Ren, C. Zhang, J. Zhou and Y. Wang, Block copolymer coated carbon nanotube membrane anodes for enhanced and multipurpose hybrid capacitive deionization, *Desalination*, 2021, **520**, 115368.
19 W.-T. Chang, P.-A. Chen, W.-R. Chen, S.-H. Liu and H. P. Wang, Simultaneous capacitive deionisation and disinfection of saltwater by Ag@C/rGO electrodes, *Environ. Chem.*, 2022, **18**, 352–359.
20 R. Bahru, N. Shaari and M. A. Mohamed, Allotrope carbon materials in thermal interface materials and fuel cell applications: A review, *Int. J. Energy Res.*, 2020, **44**, 2471–2498.
21 S. Zhang, B. Cheng, Z. Gao, D. Lan, Z. Zhao, F. Wei, Q. Zhu, X. Lu and G. Wu, Two-dimensional nanomaterials for high-efficiency electromagnetic wave absorption: an overview of recent advances and prospects, *J. Alloys Compd.*, 2022, **893**, 162343.
22 N. Fatima, U. Y. Qazi, A. Mansha, I. A. Bhatti, R. Javaid, Q. Abbas, N. Nadeem, Z. A. Rehan, S. Noreen and M. Zahid, Recent developments for antimicrobial applications of graphene-based polymeric composites: A review, *J. Ind. Eng. Chem.*, 2021, **100**, 40–58.
23 H. Ji, H. Sun and X. Qu, Antibacterial applications of graphene-based nanomaterials: recent achievements and challenges, *Adv. Drug Delivery Rev.*, 2016, **105**, 176–189.
24 H. Mohammed, A. Kumar, E. Bekyarova, Y. Al-Hadeethi, X. Zhang, M. Chen, M. S. Ansari, A. Cochis and L. Rimondini, Antimicrobial mechanisms and effectiveness of graphene and graphene-functionalized biomaterials. A scope review, *Front. Bioeng. Biotechnol.*, 2020, **8**, 465.
25 M. A. Wahab, L. Li, H. Li and A. Abdala, Silver nanoparticle-based nanocomposites for combating infectious pathogens: recent advances and future prospects, *Nanomaterials*, 2021, **11**, 581.
26 L. Rizzello and P. P. Pompa, Nanosilver-based antibacterial drugs and devices: mechanisms, methodological drawbacks, and guidelines, *Chem. Soc. Rev.*, 2014, **43**, 1501–1518.
27 S. Agrawal, M. Bhatt, S. K. Rai, A. Bhatt, P. Dangwal and P. K. Agrawal, Silver nanoparticles and its potential applications: A review, *J. Pharmacogn. Phytochem.*, 2018, **7**, 930–937.
28 B. Rajashekhar, G. Pandey, R. Sekar and M. Veerapandian, Electro Co-deposition of Copper-Silver Nanocrystallite Alloy Cluster: A way for Tunable SERS Substrate Development, *Mater. Lett.: X*, 2022, 100157.
29 J. Biener, A. Wittstock, T. F. Baumann, J. Weissmüller, M. Bäumer and A. V. Hamza, Surface chemistry in nanoscale materials, *Materials*, 2009, **2**, 2404–2428.
30 P.-A. Chen, H.-C. Cheng and H. P. Wang, Activated carbon recycled from bitter-tea and palm shell wastes for capacitive desalination of salt water, *J. Cleaner Prod.*, 2018, **174**, 927–932.
31 C.-H. Huang, H. P. Wang, J.-E. Chang and E. M. Eyring, Synthesis of nanosize-controllable copper and its alloys in carbon shells, *Chem. Commun.*, 2009, 4663–4665.
32 S. Mittapally, R. Taranum and S. Parveen, Metal ions as antibacterial agents, *J. Drug Delivery Ther.*, 2018, **8**, 411–419.
33 A. A. Yaqoob, K. Umar and M. N. M. Ibrahim, Silver nanoparticles: various methods of synthesis, size affecting factors and their potential applications-a review, *Appl. Nanosci.*, 2020, **10**, 1369–1378.
34 M. Radetić and D. Marković, Nano-finishing of cellulose textile materials with copper and copper oxide nanoparticles, *Cellulose*, 2019, **26**, 8971–8991.
35 M. B. Đolić, V. N. Rajaković-Ognjanović, S. B. Štrbac, S. I. Dimitrijević, M. N. Mitrić, A. E. Onjia and L. V. Rajaković, Natural sorbents modified by divalent $Cu^{2+}$-and $Zn^{2+}$-ions and their corresponding antimicrobial activity, *New Biotechnol.*, 2017, **39**, 150–159.
36 J. Mahin and L. Torrente-Murciano, Continuous synthesis of monodisperse iron@ iron oxide core@ shell nanoparticles, *Chem. Eng. J.*, 2020, **396**, 125299.
37 D. Chen, J. Shi and H. Shen, High-dispersed catalysts of core-shell structured $Au@SiO_2$ for formaldehyde catalytic oxidation, *Chem. Eng. J.*, 2020, **385**, 123887.
38 Y. Wu, Y. Zhang, X. Lv, C. Mao, Y. Zhou, W. Wu, H. Zhang and Z. Huang, Synthesis of polymeric ionic liquids mircrospheres/Pd nanoparticles/$CeO_2$ core-shell structure catalyst for catalytic oxidation of benzyl alcohol, *J. Taiwan Inst. Chem. Eng.*, 2020, **107**, 161–170.
39 J. Guerrero-Contreras and F. Caballero-Briones, Graphene oxide powders with different oxidation degree, prepared by synthesis variations of the Hummers method, *Mater. Chem. Phys.*, 2015, **153**, 209–220.
40 C. N. R. Rao, A. E. K. Sood, K. E. S. Subrahmanyam and A. Govindaraj, Graphene: the new two-dimensional nanomaterial, *Angew. Chem., Int. Ed.*, 2009, **48**, 7752–7777.
41 T. N. Tuan, S. Chung, J. K. Lee and J. Lee, Improvement of water softening efficiency in capacitive deionization by ultra purification process of reduced graphene oxide, *Curr. Appl. Phys.*, 2015, **15**, 1397–1401.
42 L. Chang and Y. H. Hu, Surface-microporous graphene for high-performance capacitive deionization under ultralow saline concentration, *J. Phys. Chem. Solids*, 2019, **125**, 135–140.